On the onset of oscillatory convection in molten gallium

B. Hof, A. Juel, L. Zhao, Daniel Henry, H. Ben Hadid, T. Mullin

J. Fluid Mech. (2004), *vol.* 515, *pp.* 391–413.
DOI: 10.1017/S0022112004000527 Printed in the United Kingdom

On the onset of oscillatory convection in molten gallium

By B. HOF[1], A. JUEL[2], L. ZHAO[3], D. HENRY[3], H. BEN HADID[3] AND T. MULLIN[1]

[1]Schuster Laboratory, The University of Manchester, Manchester M13 9PL, UK
[2]Department of Mathematics, The University of Manchester, Manchester M13 9PL, UK
ajuel@ma.man.ac.uk
[3]Laboratoire de Mécanique des Fluides et d'Acoustique UMR 5509, Ecole Centrale de Lyon/Université Claude Bernard Lyon 1, ECL, BP 163, 69131 Ecully Cedex, France

(Received 18 July 2003 and in revised form 2 June 2004)

The results of experimental and numerical investigations of the onset of oscillatory convection in a sidewall heated rectangular cavity of molten gallium are reported. Detailed comparisons are made between experimental observations and calculations from numerical simulations of a three-dimensional Boussinesq model. The onset of time-dependence takes place through supercritical Hopf bifurcations and the loci of critical points in the (Gr, Pr)-plane are qualitatively similar with excellent agreement between the frequencies of the oscillatory motion. This provides a severe test of the control of the experiment since the mode of oscillation is extremely sensitive to imperfections.

Detailed numerical investigations reveal that there are a pair of Hopf bifurcations which exist on two asymmetric states which themselves arise at a subcritical pitchfork from the symmetric state. There is no evidence for this in the experiment and this qualitative difference is attributed to non-Boussinesq perturbations which increase with Gr.

However, the antisymmetric spatial structure of the oscillatory state is robust and is present in both the experiment and the numerical model. Moreover, the detailed analysis of the numerical results reveals the origins of the oscillatory instability.

1. Introduction

Sidewall convection is an established heat and mass transfer problem of significance in both fundamental fluid mechanics and engineering applications such as crystal growth (Müller & Ostrogorsky 1993). A wide variety of flow fields can be generated depending on the geometry of the enclosure, properties of the fluid, boundary conditions, external fields (gravity, electric and/or magnetic fields) and the presence of phase changes. In the case of a flow in a rectangular cavity, the basic flow is a simple unicellular circulation, where motion is up the hot wall, across the top, down the cold wall and returning along the bottom. When the horizontal temperature gradient is increased, however, the flow becomes unsteady and eventually turbulence sets in for large temperature differences. The evolution of the flow depends sensitively on the details of the system.

Our interest is in the first onset of time-dependence in such convective flows, with relevance to metallic or semi-conductor materials processing. In practical flows,

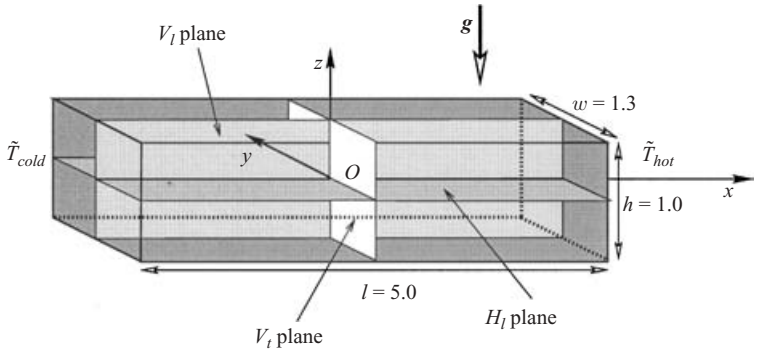

FIGURE 1. Geometry of the laboratory model flow.

instabilities in the melt phase during crystal growth can be frozen into the solid product and degrade the performance of semi-conductor devices (Hurle 1966). The melts are good thermal conductors, so that the Prandtl number, Pr (the ratio of the viscous to the thermal diffusivity), is small and heat is transported primarily by conduction. Our laboratory model flow is contained in an insulated enclosure of rectangular cross-section, where the endwalls are conducting. It has relative dimensions length = 5.0, width = 1.3 and height = 1.0, where all dimensions are scaled by the dimensional height. The geometry is shown in figure 1. The working fluid is gallium with $Pr \sim 0.02$ and the flow is driven by differentially heating the ends to impose a horizontal temperature difference $\tilde{T}_{hot} - \tilde{T}_{cold}$, while keeping the mean temperature, $T_m = (\tilde{T}_{hot} + \tilde{T}_{cold})/2$, constant. In addition to Pr and the aspect ratios, a third governing parameter is the Grashof number, Gr, which is a measure of the relative importance of buoyancy and viscous forces, and hence is proportional to the applied temperature difference.

The first experimental work on this problem is reported by Hurle, Jakeman & Johnson (1974), who investigate the transition to unsteady convection in rectangular open cavities of moderate aspect ratios (typically of relative dimensions $2.5 \times 1.1 \times 1.0$), filled with gallium. They show that the critical thresholds for the onset of oscillatory convection are reduced when the cavity length is increased, raised when the depth is increased and, importantly, also raised when an external magnetic field is applied. Hart (1983) reports measurements of the critical Grashof number Gr_c, frequency and wavelength at the onset of oscillatory flow in a large-aspect-ratio cell ($17.5 \times 17.5 \times 1.0$) filled with mercury. He finds good agreement with an analytical model derived for infinitely extended layers and confirms that the dominant instability is to rolls with axes parallel to the temperature gradient.

Further experimental studies were conducted in connection with the numerical benchmark problem proposed in a GAMM workshop by Roux (1990). Pratte & Hart (1990) and Hart & Pratte (1990) consider closed cavities filled with mercury, of aspect ratios $4 \times 1 \times 1$, $4 \times 2 \times 1$ and $8 \times 8 \times 1$. They demonstrate the stabilizing influence of the sidewalls on the transition to oscillatory flow. For aspect ratios $4 \times 2 \times 1$ and $8 \times 8 \times 1$, time-dependent flows in the form of standing waves are obtained at Grashof numbers 4.23×10^4 and 2.22×10^4, respectively. However, for the $4 \times 1 \times 1$ case, the instability onset does not occur until $Gr = 1.69 \times 10^5$. A similar stabilizing effect of the sidewalls is reported by Hung & Andereck (1990) who observe the transition to oscillatory convection in mercury for cavities with aspect ratios $4 \times 1 \times 1$ and $4 \times 2 \times 1$

at $Gr = 1.5 \times 10^5$ and $Gr = 3.9 \times 10^4$, respectively. For a larger-aspect-ratio cavity of $17.9 \times 17.8 \times 1.0$, Hung & Andereck (1988) obtain oscillatory longitudinal modes in qualitative agreement with Hart (1983). However, the observed critical Grashof numbers are far in excess of those expected from theory and this is explained by the prior emergence of transverse stationary rolls which are not present in the theoretical model.

Kamotani & Sahraoui (1990) report an extensive study of the effects of aspect ratio on the onset of oscillations in mercury. They establish that the critical Grashof number increases as the length is decreased, but find that changes in the width have a lesser influence on the onset of time-dependence. The threshold, however, also decreases as the width is increased and a minimum is obtained for a width of approximately five times the depth. They also point out that the amplitude of the oscillation is greater near the endwalls. More recently, Braunsfurth & Mullin (1996) established that the onset of time-dependence takes place through a super-critical Hopf bifurcation. They observe an overall increase in the critical Grashof number with increasing Pr for a gallium-filled cavity of aspect ratios $4.0 \times 1.3 \times 1.0$. In addition, they find four different modes of oscillation at onset in the parameter range between $Pr = 0.016$ and $Pr = 0.022$. Juel *et al.* (2001) report investigations of the spatial nature of the oscillation for a similar situation (aspect ratios $5.0 \times 1.3 \times 1.0$) and find a 180° phase shift between the measurements of temperature oscillations taken close to the left-hand sidewall and those taken close to the right-hand sidewall. Furthermore, temperature time-series sampled halfway between these two sidewalls display oscillations of smaller amplitude, with a frequency twice that measured in other locations.

The first theoretical predictions of the stability of flows driven by horizontal temperature gradients in conducting fluids are reported for the one-dimensional parallel flow in an infinitely extended layer, known as the Hadley circulation. For rigid upper and lower boundaries, Hart (1972, 1983) determines the sensitivity of such flows to both transverse and longitudinal disturbances (corresponding, respectively, to perturbation rolls with axis perpendicular and parallel to the temperature gradient), whereas Gill (1974) focuses specifically on longitudinal disturbances. These results are refined by Laure (1987) and Kuo & Korpela (1988) who find that for adiabatic boundaries, the first transition is to steady transverse rolls for $Pr < 0.033$, and to oscillatory longitudinal rolls for $0.033 \leqslant Pr < 0.2$. This work is subsequently extended by nonlinear analysis and for situations with an upper free surface (Wang & Korpela 1989; Laure & Roux 1990).

These predictions for the Hadley circulation, although interesting, are in fact of limited relevance to the study of the oscillatory transitions in finite rectangular cavities. For example, as shown at the GAMM workshop (Roux 1990), the Hadley circulation is not the appropriate base flow for the domain, at values of Gr at which oscillations occur. Direct numerical simulations are thus required to appropriately model the high Gr regime. Calculations performed at the GAMM workshop for two-dimensional cavities of aspect ratio 4 (length over height) show a first transition to stationary co-rotating cells, followed by a Hopf bifurcation corresponding to an oscillatory solution between a one-cell and three-cell state. Winters (1988) used a continuation method to follow the path of Hopf bifurcation points and finds that it increases strongly with Pr from the value at $Pr = 0$. Skeldon, Riley & Cliffe (1996) extend this work by varying the aspect ratio and the inclination of the box. These two-dimensional results are believed to be relevant for cavities with a relatively large width, but may be less so for the confined cavities of interest here.

Afrid & Zebib (1990) solve the three-dimensional problem for cavities with aspect ratios $4 \times 1 \times 1$ and $4 \times 2 \times 1$ and $Pr = 0$, where they assume a symmetry with respect to the longitudinal vertical plane. However, this assumption is not in accord with the experimental results of Pratte & Hart (1990). Henry & Buffat (1998) study the oscillatory transition in a $4 \times 2 \times 1$ cavity for $Pr = 0$ and $Pr = 0.026$. They find that the transition occurs through a symmetry-breaking Hopf bifurcation giving rise to a roll oscillation. Good agreement is found for thresholds and flow symmetries with the experimental results of Hart & Pratte (1990), Pratte & Hart (1990) and Hung & Andereck (1990). A more recent study by Wakitani (2001) considers a large variety of cavities with lengthwise aspect ratios between 2 and 4 and widthwise aspect ratios between 0.5 and 4.2. The onset of oscillation is investigated as a function of aspect ratios and Pr in the range $0 \leqslant Pr \leqslant 0.027$. It is found that the thresholds globally increase both with Pr and the reduction of the widthwise aspect ratio. However, these variations are not regular, indicating changes in the oscillatory modes at onset.

Thus far, there have been few attempts at quantitative comparisons between experimental and three-dimensional numerical results for the transition to time-dependence. Here, we present the results of a detailed, comparative study between numerical and experimental results for the onset of oscillatory flow in a gallium-filled cavity of aspect ratios $5.0 \times 1.3 \times 1.0$. This approach enables us to gain a detailed understanding of the convective flow, and also raises questions regarding the relevance of the traditional Boussinesq model to flows of practical interest. The paper is organized as follows. The model equations and the numerical techniques are described in § 2 and experimental details are presented in § 3. In § 4.1, a comparison between experimental and numerical onset of oscillatory flow for $Pr = 0.0205$ establishes excellent overall agreement, but also points to some differences. A further investigation of the dependence of the transition to time-dependent flow on Pr is then discussed in § 4.2. The spatial dynamics of the oscillatory flow are analysed in § 4.3 where it is shown that numerical and experimental oscillatory modes are in excellent quantitative agreement. An interesting bifurcation scenario involving a subcritical symmetry-breaking bifurcation prior to a pair of supercritical Hopf bifurcations is obtained numerically, whereas the experimental results give a direct supercritical transition to oscillatory flow. Our claim is that this qualitative difference can be explained by the symmetry of the Boussinesq model used in the numerical simulations.

2. Mathematical model and numerical techniques

The mathematical model comprises a rectangular parallelepiped cavity filled with a low-Prandtl-number conducting and incompressible fluid, and no-slip boundary conditions are applied along all walls. The cavity has aspect ratios $5.0 \times 1.3 \times 1.0$, i.e. $A_x = l/h = 5.0$ and $A_y = w/h = 1.3$, where l is the length of the cavity (along x), h is its height (along z) and w its width (along y), as shown schematically in figure 1. The thermal boundary conditions are such that the sidewalls are adiabatic and the vertical ends are isothermal and held at different temperatures, $\tilde{T}_{hot}$ at the right and $\tilde{T}_{cold}$ at the left-hand endwall, respectively. This generates a horizontal temperature gradient which drives a convective circulation within the cavity.

The fluid is assumed to be Newtonian with constant kinematic viscosity ν, thermal diffusivity κ. The usual Boussinesq approximation is applied such that density variations are restricted to the buoyancy term. Specifically, the linear law, $\rho = \rho_m(1 - \beta(\tilde{T} - T_m))$, where β is the thermal expansion coefficient, T_m is a reference temperature taken as the mean temperature $(\tilde{T}_{hot} + \tilde{T}_{cold})/2$ and ρ_m is the density at the reference

temperature, is used. The convective motion is modelled by the Navier–Stokes equations coupled to an energy equation. Using h, h^2/ν, ν/h, $\rho_m \nu^2/h^2$ and $\gamma = (\tilde{T}_{hot} - \tilde{T}_{cold})/A_x$ as scales for length, time, velocity, pressure and temperature, respectively, these equations are:

$$\nabla \cdot \boldsymbol{u} = 0,$$
$$\frac{\partial \boldsymbol{u}}{\partial t} + (\boldsymbol{u} \cdot \nabla)\,\boldsymbol{u} = -\nabla p + \nabla^2 \boldsymbol{u} + Gr\, T\, \boldsymbol{e}_z,$$
$$\frac{\partial T}{\partial t} + (\boldsymbol{u} \cdot \nabla)\, T = \frac{1}{Pr} \nabla^2 T,$$

with boundary conditions

$$\partial T/\partial z = 0 \quad \text{on} \quad z = \pm 1/2, \quad \partial T/\partial y = 0 \quad \text{on} \quad y = \pm A_y/2,$$

$$T = -A_x/2 \quad \text{on} \quad x = -A_x/2, \quad T = A_x/2 \quad \text{on} \quad x = A_x/2,$$

and

$$\boldsymbol{u} = 0 \quad \text{on all boundaries.}$$

The dimensionless variables are the velocity vector $\boldsymbol{u} = (u, v, w)$, the pressure p and the temperature $T = (\tilde{T} - T_m)/\gamma$, $\boldsymbol{e}_z$ is the unit vector in the vertical direction, and the non-dimensional parameters are the Grashof number, $Gr = \beta g \gamma h^3/\nu^2$, where g is the acceleration due to gravity, and the Prandtl number, $Pr = \nu/\kappa = \mu c_p/k$, where μ is the dynamic viscosity, c_p is the specific heat coefficient and k is the thermal conductivity.

Henry & Buffat (1998) show that, under the Boussinesq approximation, the steady solutions obtained at moderate Gr in this geometry contain two symmetries: S is a reflection symmetry with respect to the V_l plane (left–right symmetry) and S_r is a π-rotational symmetry about the y-axis. These symmetries are defined, respectively, as:

$$S: \quad (x, y, z, t) \to (x, -y, z, t), \quad (u, v, w, T) \to (u, -v, w, T)$$

and

$$S_r: \quad (x, y, z, t) \to (-x, y, -z, t), \quad (u, v, w, T) \to (-u, v, -w, -T).$$

These two symmetries may be combined to give a global symmetry S_c with respect to the centrepoint of the cavity ($S_c = S \cdot S_r$). When increasing Gr, bifurcations to new steady or oscillatory flow states may break the symmetries. Although the idealized Boussinesq model possesses the S_r symmetry for sufficiently small Gr, this symmetry will not apply if, for instance, the diffusivities depend on temperature, as is the case in any experimental realization of this flow.

The governing equations were solved by direct numerical simulation (DNS) in a three-dimensional domain, using a spectral-element method, as described in Ben-Hadid & Henry (1997). The time discretization was carried out using the high-order splitting algorithm of Karniadakis, Israeli & Orszag (1991), and the spatial discretization was obtained using Gauss–Lobatto–Legendre point distributions. All the simulations were performed with a $36 \times 16 \times 18$ mesh and double-precision arithmetic. This is the optimal mesh available for the unsteady calculations using current computing resources; it is a compromise between numerical accuracy and practical computing times. The computations were carried out on an NEC-SX5 computer. Each time step required approximately 2 s of CPU time, and thus the calculation of an oscillatory flow from the initial conditions of no flow took, on average, 14 h.

Mesh	u_{max}	w_{max}	v_{max}
$18 \times 9 \times 8$	1.21713	0.492896	0.209445
$27 \times 14 \times 12$	1.25907	0.504150	0.258032
$36 \times 18 \times 16$	1.25223	0.522751	0.272872
$54 \times 28 \times 24$	1.25873	0.539128	0.272584
$72 \times 36 \times 32$	1.26502	0.540228	0.272034

TABLE 1. Mesh refinement tests of numerical accuracy of the calculated steady flow at $Gr = 37\,500$ and $Pr = 0.0188$. Convergence is observed for relatively refined grids of at least $36 \times 18 \times 16$. The maximum velocity components u_{max}, w_{max} and v_{max} vary by 1.0%, 3.0% and 0.3%, respectively, as the $36 \times 18 \times 16$ mesh is doubled in size in all directions. These small differences are, in fact, overestimates, since the maximum values of the flow will not generally lie on the nodes of the mesh. By comparison, the absolute variations as the grid is doubled from $18 \times 9 \times 8$ to $36 \times 18 \times 16$ are 2.9%, 6.0% and 30%.

The code was successfully tested by comparison with results from Ben Hadid & Henry (1997). The results of mesh refinement tests performed for a steady state at $Gr = 37\,500$ and $Pr = 0.0188$ are given in table 1 where it may be seen that the steady flows are highly resolved. In addition, the symmetries of the steady states were verified with zeros of velocity and appropriate temperature profiles being resolved to values of order 10^{-10}. The thresholds Gr_c for the onset of oscillations were obtained by fitting a square root law to the amplitude of a suitable measure which was calculated at several supercritical values of Gr. With this procedure, the error on the values of Gr_c is estimated to be approximately $\Delta Gr_c = 500$.

Important information concerning the physical mechanisms involved in the transition to the oscillatory state can be obtained from kinetic energy balances estimated from the numerical results calculated above onset. From the oscillatory flow $[u, v, w, T](x, y, z, t)$ (or $[u_i, T](x_i, t)$), the fluctuations u_i', T' are obtained using the Reynolds decomposition, $u_i = \bar{u}_i + u_i'$, $T = \bar{T} + T'$, where $\bar{u}_i$, $\bar{T}$ are time-averaged values over one period of oscillations. The fluctuating kinetic energy is then defined as:

$$k = \tfrac{1}{2} u_i' \, u_i',$$

and the volume integrated fluctuating kinetic energy as:

$$K = \int_{\Omega} \tfrac{1}{2} u_i' \, u_i' \, \mathrm{d}\Omega.$$

Close to the threshold, the Reynolds–Orr equation can then be written for the rate of change of the total fluctuating kinetic energy:

$$\frac{\partial K}{\partial t} = E_{shear} + E_{visc} + E_{buoy} \tag{2.1}$$

where

$$E_{shear} = -\int_{\Omega} u_i' \, u_j' \, \frac{\partial \bar{u}_i}{\partial x_j} \, \mathrm{d}\Omega,$$

$$E_{visc} = -\int_{\Omega} \left(\frac{\partial u_i'}{\partial x_j} \right)^2 \mathrm{d}\Omega,$$

$$E_{buoy} = Gr \int_{\Omega} u_i' \, T' \, \delta_{i3} \, \mathrm{d}\Omega.$$

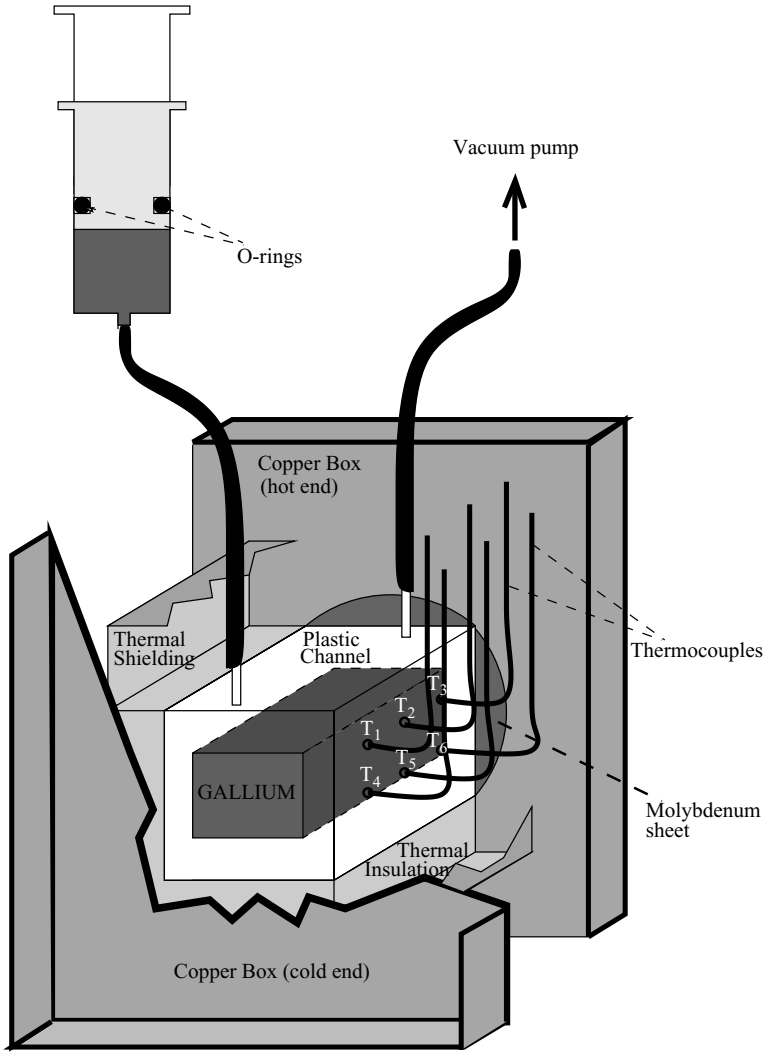

FIGURE 2. Experimental apparatus.

E_{shear} represents the production of fluctuating kinetic energy by shear of the mean flow, E_{visc} the viscous dissipation of fluctuating kinetic energy, and E_{buoy} the production of fluctuating kinetic energy by buoyancy. The calculation of all these terms enables us to determine which contributions are predominantly responsible for the triggering of the instability through production of fluctuating kinetic energy.

3. Experimental methods

A detailed description of the experimental apparatus is given in Hof, Juel & Mullin (2003). Therefore, we will only discuss essential details here. The apparatus is shown schematically in figure 2. The sample of liquid gallium was held in an insulated enclosure of rectangular cross-section, which was 5.0 cm long, 1.3 cm wide and 1.0 cm high. The conducting endwalls were made of 1 mm thick molybdenum sheets, which have a thermal conductivity of approximately five times that of gallium and, importantly, are impervious to attack by it. The insulated enclosure had 5 mm

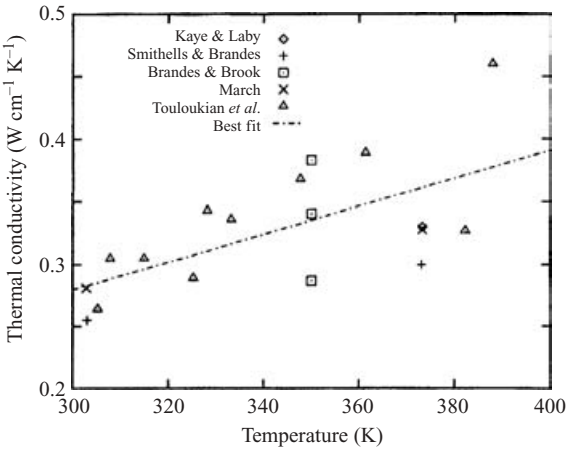

FIGURE 3. Temperature dependence of the thermal conductivity of gallium (from Braunsfurth *et al.* 1997).

thick walls and was machined from Lexan, a transparent plastic, whose thermal conductivity is 150 times smaller than that of gallium.

Great care was taken to ensure that the cell was completely filled with gallium and sealed from the outside environment. Thus, the gallium wetted all surfaces and oxidation of the sample was avoided. Each molybdenum endwall was inset into the side of a copper box through which silicone oil, held at constant temperature, was circulated. The oil temperature was controlled to within ± 0.01 K by commercial circulator baths. The experiment was further enclosed in a cabinet, whose temperature was controlled to within 308.0 ± 0.5 K.

In order to minimize heat losses from the gallium-filled cell to the surroundings, the cavity was thermally shielded as described in Hof *et al.* (2003). This intricate level of experimental control was necessary to ensure the S_r symmetry of the steady, experimental temperature field to within measurement error. Thus, the steady base flow generated by the present experimental set-up is in close agreement with the numerical model.

The material properties of gallium depend on temperature, so that *Gr* and *Pr* are both functions of temperature. Accurate estimates of the viscosity and density of gallium are quoted by Braunsfurth & Mullin (1996). The temperature dependence of the viscosity is given by

$$\eta = 0.4359 \exp\left(\frac{481}{\tilde{T}}\right) \times 10^{-3}\,\mathrm{N\,s\,m^{-2}},$$

and the temperature dependence of density is

$$\rho = (6.32723 - 7.3743 \times 10^{-4}\,\tilde{T} + 1.37767 \times 10^{-7}\,\tilde{T}^2) \times 10^3\,\mathrm{kg\,m^{-3}},$$

where $\tilde{T}$ is the temperature in Kelvin. However, the dependence of thermal conductivity is less well known, since the measurements available in the literature display significant scatter. We use the temperature dependence of k collated by Braunsfurth *et al.* (1997) and shown in figure 3. These measurements were collected from Brandes & Brook (1992), Smithells & Brandes (1976), Kaye & Laby (1982), March (1968) and Touloukian *et al.* (1979). A linear least-squares fit to the data shows that

$$k = (0.11\,\tilde{T} - 5) \pm 4\,\mathrm{W\,m^{-1}\,K^{-1}},$$

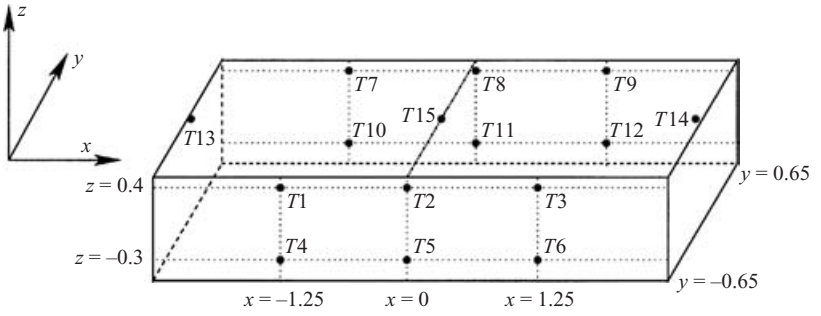

FIGURE 4. Location of the experimental temperature probes.

and consequently, there is an absolute error in the value of the experimental Prandtl number of approximately 16%. The temperature dependence of k recommended by Mills, Monaghan & Keene (1996) of the National Physical Laboratory yields experimental Prandtl numbers approximately 6% larger than those quoted here.

The experimental values of Gr and Pr were determined based on the mean temperature in the cavity $T_m = (\tilde{T}_{hot} + \tilde{T}_{cold})/2$. The maximum (minimum) Prandtl numbers available were $Pr_{max} = 0.022$ ($Pr_{min} = 0.0154$) which were reached for mean temperatures of 332 K (376 K), respectively. These limits are imposed by the freezing point of gallium (302.9 K) and the upper working temperature of Lexan (383 K).

Measurements of the convective flow were taken with 15 type K thermocouple probes of diameter 0.25 mm inserted by 1 mm into the gallium at the positions shown in figure 4 ($y = \pm 0.55$ for probes 1 to 12). All thermocouples were carefully calibrated prior to use, which enabled temperatures to be measured to an accuracy of ± 0.01 K. The sampling of the data and the temperature settings of the circulators were fully automated and under computer control. Typically, temperatures were increased (decreased) in steps of 0.1 K at the hot (cold) end, respectively, which yielded a variation in Grashof of $\Delta Gr = 300$, while the mean temperature was kept constant. The flow was left to settle for 1 h between increments and temperatures were sampled for a further 30 min at a frequency of 5 Hz. A fast Fourier transform (FFT) was performed on each recorded time series and a time-dependent flow was deemed to exist when a peak of the FFT was in excess of ten times the background noise level. This method enabled us to determine the onset of oscillations very accurately, so that the error on the critical value of the Grashof number, Gr_c, is less than one step size (typically $\Delta Gr = 300$).

4. Results

4.1. *Comparison between experimental and numerical onset for* $Pr = 0.0205$

The transition to time-dependent flow in the experiment was initially investigated by setting the value of the Prandtl number to $Pr = 0.0205$ (corresponding to a set mean temperature of 338 K), and increasing the Grashof number from zero in steps of $\Delta Gr_{exp} = 380$. The steady flow loses stability to a time-periodic flow at $Gr_c(\text{exp}) = 42\,500$. A typical bifurcation diagram is shown in figure 5(a), where the standard deviation of the temperature oscillatory signal $T3$ is plotted against the excess parameter $\epsilon_{exp} = Gr/Gr_c(\text{exp}) - 1$. A square-root dependence on ϵ_{exp} is found close to the critical point ($\epsilon_{exp} = 0$), which suggests that the transition to time-dependence takes place through a supercritical Hopf bifurcation in accordance with previous

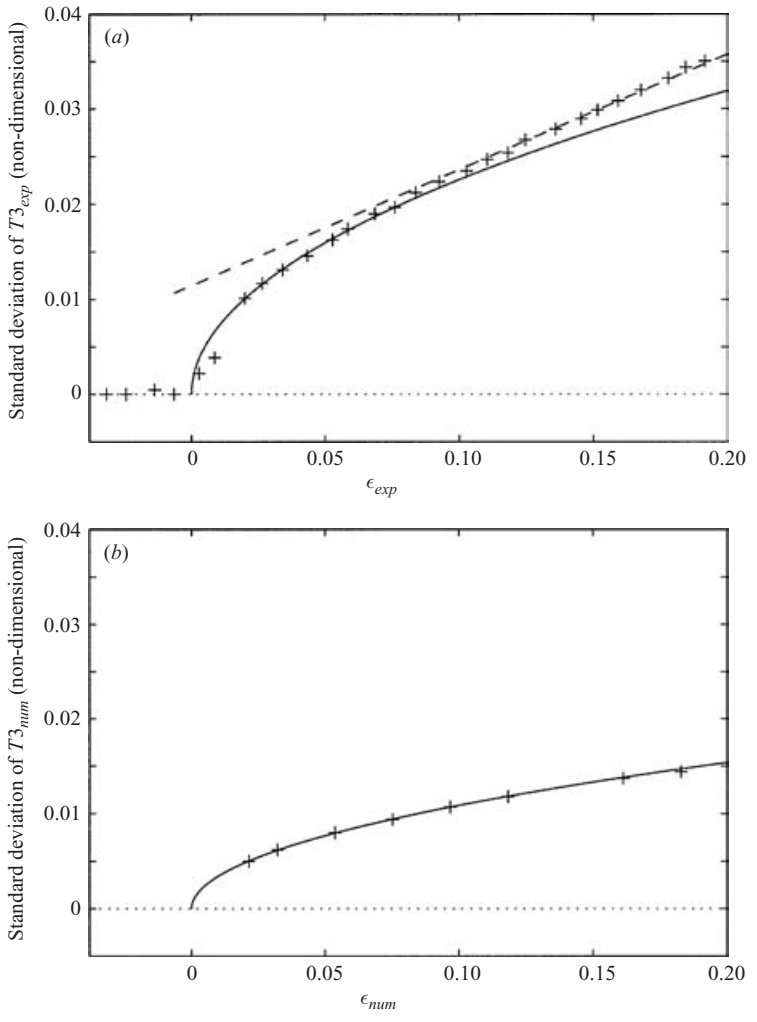

FIGURE 5. Bifurcation diagrams for $Pr = 0.0205$: standard deviation of the non-dimensional temperature oscillation $T3$ versus the excess parameter, $\epsilon = Gr/Gr_c - 1$: (*a*) +, experimental data; —, square-root fit; – – –, linear fit; $Gr_c(\text{exp}) = 42\,500$; (*b*) +, numerical data; —, square-root fit; $Gr_c(\text{num}) = 46\,500$.

results by Henry & Buffat (1998), Braunsfurth & Mullin (1996) and Hof & Mullin (2001). Hence, the critical value of the Grashof number, $Gr_c(\text{exp})$, was determined using a fit, as illustrated in figure 5(*a*). Nonlinear effects become important when $\epsilon_{exp} > 0.1$, and the amplitude grows linearly with ϵ_{exp}. This behaviour was observed consistently for all the probes.

In the numerical calculations, the flow was initially calculated for $Gr = 60\,000$, where it was found to be time-dependent but disordered. The Grashof number was then reduced to $Gr = 56\,000$ and the flow became periodic. Subsequent calculations were performed in eight steps of Gr down to $Gr = 47\,500$, which is 2.1% above the bifurcation point as can be seen in figure 5(*b*). Each of these simulations was run for 10^4 iterations which corresponds to approximately seventeen periods of oscillation. When the Grashof number was further decreased, a constant-amplitude oscillation

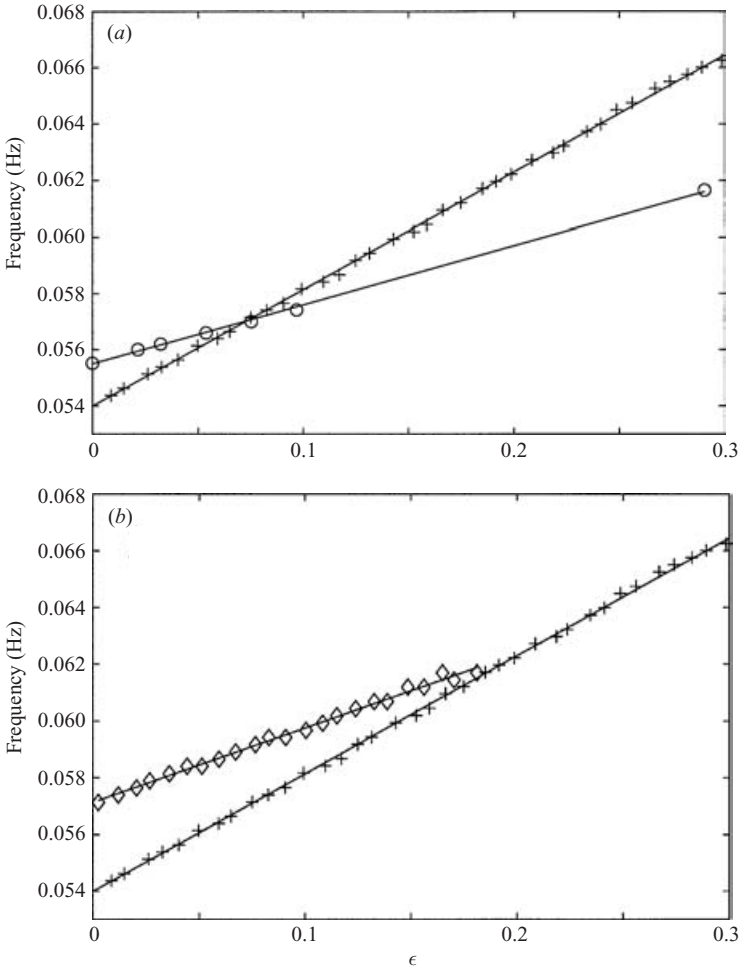

FIGURE 6. Frequency of oscillation close to onset for $Pr = 0.0205$: (*a*) comparison between experimental data (+) and numerical data (○); (*b*) comparison between the above experimental data (+), measured in a fully filled enclosure, and data taken in a cavity with a small air bubble present (◇). At onset, the experimental and numerical frequencies differ by 2.8%. The vertical axis spans 1.3×10^{-3} Hz, i.e. only 2% of the mean frequency shown in the graph.

could not be reached within 10^4 iterations because of the long time scales which result from critical slowing down close to a Hopf bifurcation point (Strogatz 1994). The standard deviation of $T3$ is plotted against ϵ_{num} in figure 5(*b*), where it may be seen that the amplitude of oscillation follows a square-root dependence on the Grashof number near onset, although the growth is somewhat slower than in the experiment. This behaviour is in agreement with the experiment and provides further evidence for a supercritical Hopf bifurcation. The bifurcation point was determined in the same way as for the experiments and the critical Grashof number obtained numerically for $Pr = 0.0205$ is $Gr_c(\text{num}) = 46\,500$.

Thus, the value of Gr_c obtained from the calculations is approximately 10% larger than in the experiment. A comparison between experimental and numerical values of the frequency of the oscillation near onset is shown in figure 6(*a*). They are in excellent agreement, i.e. in the experiment, the period of oscillation is 18.5 s at

Pr	0.014	0.016	0.019	0.0205	0.0225	0.025
Gr_c(num)	49470	47290	46360	46500	47780	51320

TABLE 2. Critical Grashof numbers determined numerically for various values of Pr within the experimental range.

onset compared to 18.1 s in the numerical simulations. In both cases, the frequency increases linearly with ϵ in the vicinity of the bifurcation point, albeit at slightly different rates. Experimentally, the sensitivity of the oscillation to imperfections in the boundary conditions was tested by injecting a small air bubble into the cell. As shown in figure 6(*b*), the frequency of oscillation increased slightly, but, most importantly, the frequency gradient with respect to ϵ decreased by a factor of two. Thus, the frequency growth beyond onset is very sensitive to small perturbations in the boundary conditions of the cell. Hence, the unavoidable presence of small imperfections in the experimental boundary conditions is the likely cause of the small discrepancy between experimental and numerical results.

4.2. *The dependence of the onset of oscillations on Pr and Gr*

The stability of the flow in the $Gr-Pr$ parameter plane was investigated experimentally by seeking the critical Grashof number for fixed values of the Prandtl number. The transition to oscillatory flow was initially studied at $Pr=0.0154$, by increasing the Grashof number in steps of $\Delta Gr_{exp}=310$ and leaving the flow to settle between steps using the criteria discussed in § 3. The critical Grashof number was taken to be the first value for which oscillations were detected within 1 h, after a small step increase in Gr. Once Gr_c had been located, the mean temperature was decreased by 1.5 K in steps of 0.05 K over a period of 90 min, and this yielded an increase in Prandtl number of approximately $\Delta Pr=3\times10^{-3}$. The flow became steady and was left to reach equilibrium for 30 min, while the applied temperature difference was kept constant. The temperature difference was then increased in steps of 0.1 K until the next transition to time-dependence was detected. This procedure was subsequently repeated across the entire range of experimentally achievable Prandtl numbers. The experimental results are presented in figure 7(*a*).

Calculating Hopf bifurcation points using DNS in a fully three-dimensional flow field requires intensive computational effort and hence the number of numerically determined bifurcation points was limited to six, and they are given in table 2. These were all found using the procedure described in § 4.1.

The numerical results are shown in figure 7(*b*). We have plotted the numerical and experimental results in separate figures to highlight the qualitative agreement between the two sets of results. The qualitative agreement is good with both sets of results indicating a single broad neutral curve with a minimum at $Pr=0.019$. There is a significant increase in Gr_c(num) for $Pr\leqslant0.016$, but this is outside the available experimental range and so could not be investigated in the experiments. The rate of increase in the numerical results of Gr_c(num) found for $Pr\geqslant0.019$ is less than half that found in the experiments. It is of the same order as in the two-dimensional numerical calculations of Skeldon *et al.* (1996) for a cell of aspect ratio 4.5 although the base flows are different. The same single mode of oscillation was detected in both sets of results and the spatial characteristics of this mode are discussed in § 4.3. Furthermore, the frequency of the oscillation was found to increase continuously with Prandtl number, as shown in figure 8.

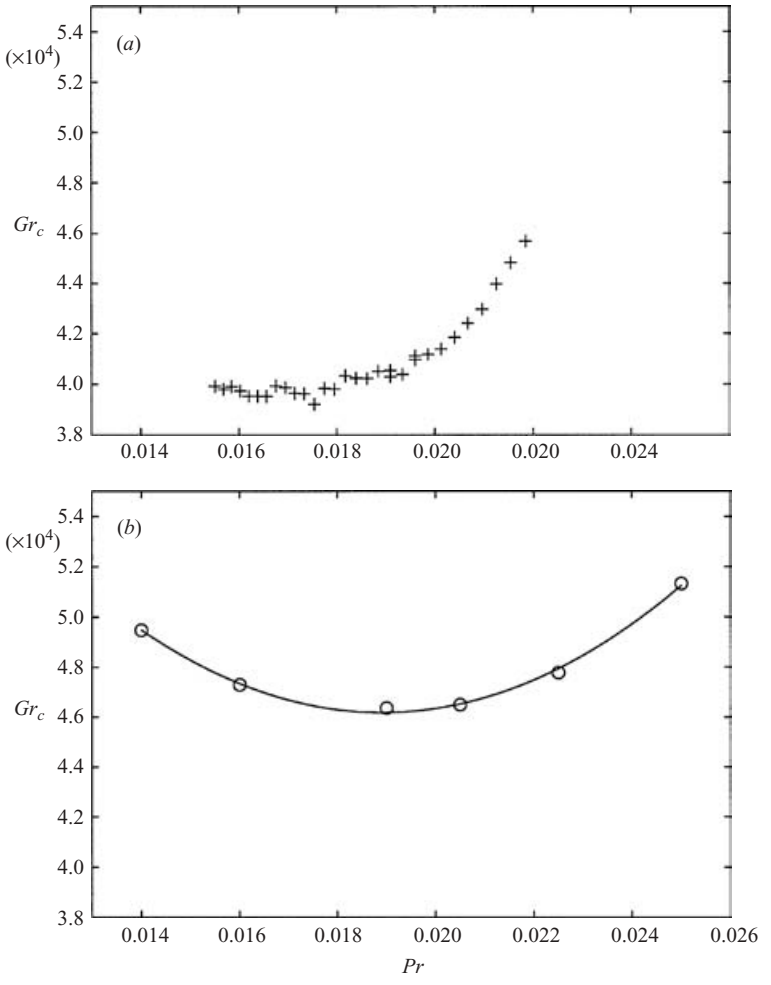

FIGURE 7. Dependence of Gr_c on the Prandtl number: (*a*) +, experimental observations; and (*b*) ○, three-dimensional numerical simulations.

Absolute comparison between the two sets of results is limited primarily by the uncertainty in the values of the physical properties. The results shown in figure 7(*b*) indicate that the oscillations set in at lower values of Gr in the experiment than in the numerical simulations over the entire range of Pr studied. In view of the uncertainty in material properties of gallium, the agreement is nevertheless satisfactory with a maximum difference between experimental and numerical results at $Pr = 0.016$ of 17%.

The experimental results indicate a significant variation of Gr_c with Pr. Thus, they readily demonstrate the importance of controlling the mean temperature in the experiment, which determines the experimental value of the Prandtl number. The critical Grashof number is clearly a continuous function of the Prandtl number over the range investigated, as oscillatory flows were not found for all parameter values (Gr, Pr) below the data.

These results are qualitatively different to those obtained in the experiments of Braunsfurth & Mullin (1996) where a similar geometry ($4.0 \times 1.3 \times 1.0$) was used.

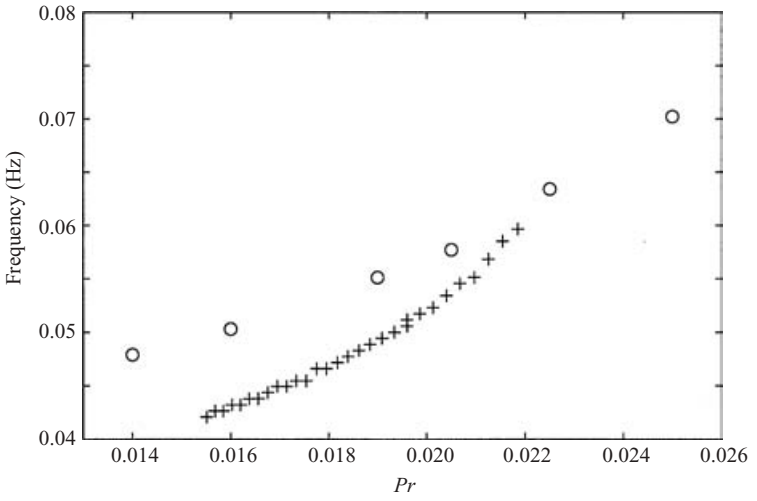

FIGURE 8. Dependence of the frequency of oscillation at onset on the Prandtl number: +, experiment; ○, numerical simulations.

They found that four distinct modes of oscillations were reproducibly observed over the same range of Pr. Furthermore, although the critical Grashof number shows an overall increase with Prandtl number in both experiments, the increase observed between $Pr = 0.016$ and $Pr = 0.022$ is approximately one order of magnitude larger in Braunsfurth & Mullin's experiment. As discussed in § 3, particular care was taken in the present experiment to ensure the accurate control of the boundary conditions. However, when the cell had not been perfectly filled and a few gas bubbles remained entrapped between the gallium and the top surface of the enclosure, a different mode was found at onset in specific parameter regimes. Two-mode interactions reminiscent of those described by Braunsfurth & Mullin (1996) were also observed. A very small amount of air, covering less than 5% of the top surface, was sufficient to lead to significant changes in the dynamics. Hence, particular care was taken throughout this study to ensure that the cell was completely filled with gallium prior to each experiment. These observations suggest that the dynamics of the convective flow are extremely sensitive to small changes in the boundary conditions, as mentioned above in § 4.1. We also believe that this sensitivity accounts for the differences with the results of Braunsfurth & Mullin (1996), as their convection cell, for instance, was not evacuated, and the top surface of the gallium sample was only loosely covered by a lid. Hence, the idealized experimental and numerical systems under study here, both exhibit dynamics which are qualitatively different from those of more practical systems, where significant imperfections in the boundary conditions are inevitable. However, the spatial structure of the oscillation remains the same, as will be discussed in § 4.3.

4.3. *Spatial dynamics of the oscillatory flow*

A first indication of the spatio-temporal structure of the oscillatory flow in the numerical and experimental results was obtained using segments of the temperature time series sampled at different locations within the cell. In figure 9, extracts of experimental and corresponding numerical time series are plotted in the left- and right-hand columns, respectively. In each graph, $T3$ is plotted with a solid line and is the reference temperature. $T6$, $T9$ and $T15$ are shown with dashed lines in the

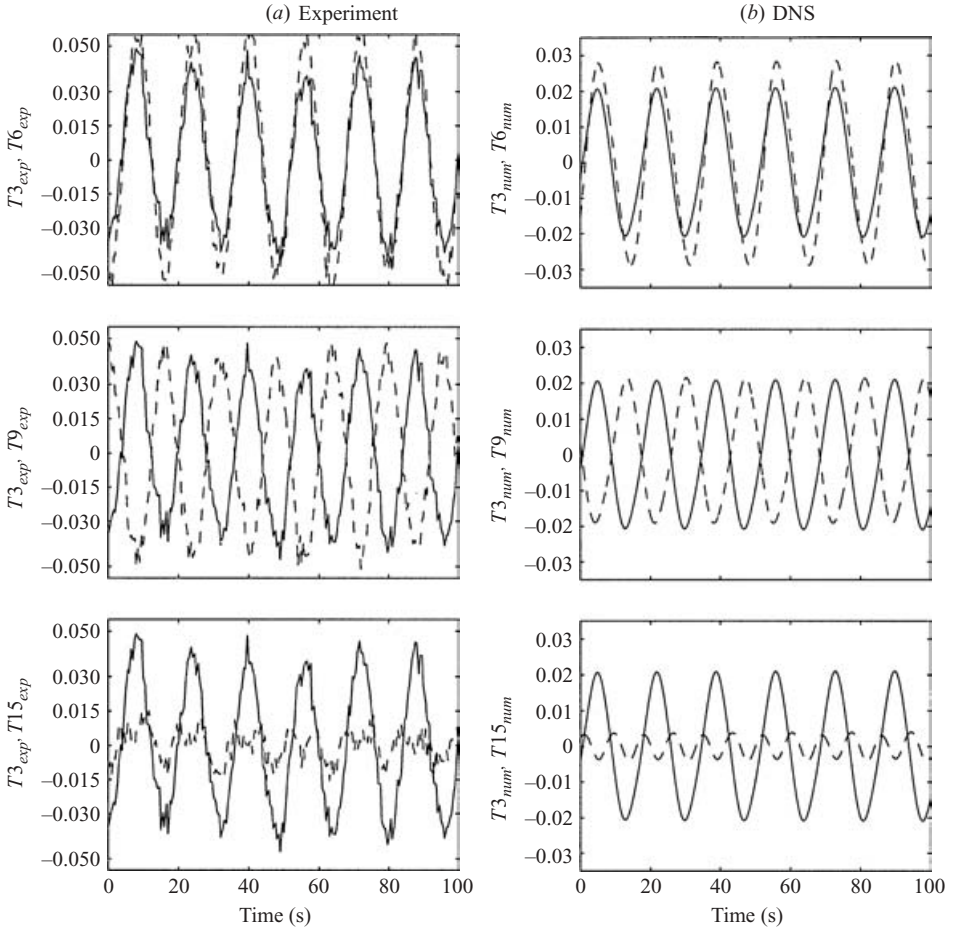

FIGURE 9. Comparison between $T3$ (solid line) and $T6$, $T9$ and $T15$ (dashed lines). The signals $T6$, $T9$ and $T15$ are plotted in the first, second and third rows, respectively. (*a*) The experimental and (*b*) the numerical time series, measured for $\epsilon \sim 0.185$.

first, second and third rows, respectively. The Prandtl number is set to $Pr = 0.019$. A relatively large value of the experimental Grashof, $Gr = 49\,100$, which corresponds to $\epsilon = 0.189$, was chosen so that a sufficient signal-to-noise ratio was obtained. The numerical time series were taken for a similar value of the bifurcation parameter of $\epsilon = 0.184$, i.e. $Gr\,(\text{num}) = 55\,000$. It is clear from figure 9 that the spatial features of the oscillation in the experiment and the numerical simulations are closely matched. The absolute values of the amplitudes of the experimental and numerical time series, e.g. $T3$, differ by a factor of approximately 1.5. However, remarkably, the amplitudes of $T6$, $T9$ and $T15$ relative to $T3$ are similar in both sets of results. This is an indication that the oscillatory flow mechanisms have the same fundamental characteristics. In addition, the temperatures measured at the locations $T3$ and $T9$ are 180° out of phase, and this phase shift was observed consistently between signals sampled on opposite lateral walls. Similarly, signals measured on the same lateral wall are closely in phase, as illustrated in figure 9 by the comparison between $T3$ and $T6$. Finally, the experimental time series sampled at $T15$, which is located near the top boundary, halfway along the length of the convection cell and halfway across its width, displays

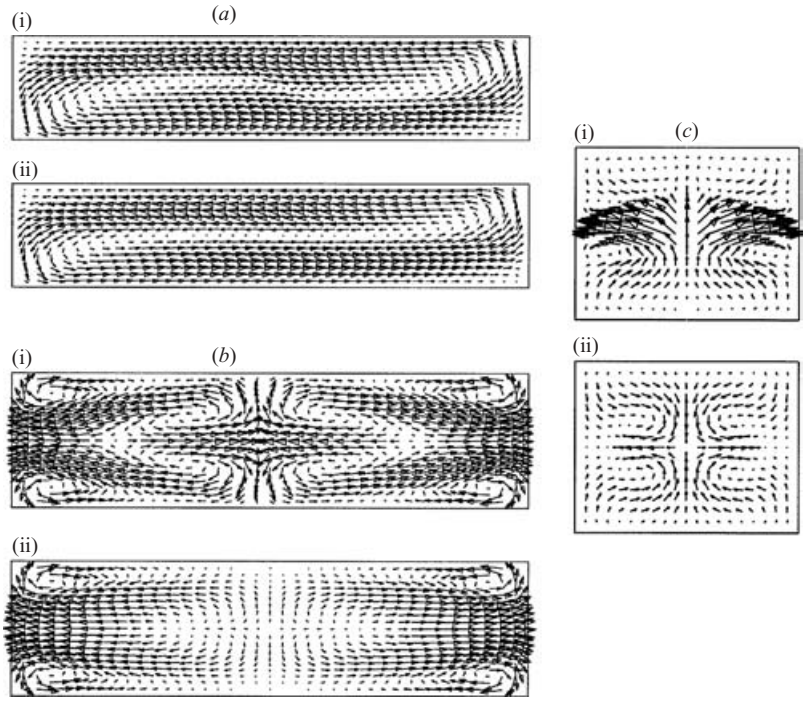

FIGURE 10. Flow field for $Gr = 49\,000$, $Pr = 0.019$: (i) oscillatory flow field averaged over one period; (ii) steady flow field. The velocity vectors are projected onto the (*a*) V_l plane, front view; (*b*) H_l plane, viewed from above; (*c*) V_t plane, viewed from the left. Both the mean flow (i) and the steady flow (ii) satisfy the S symmetry as can be seen in (*b*)(i) and (*b*)(ii). The steady flow is also S_r symmetric as shown in (*b*)(ii) and (*c*)(ii). The S_r symmetry, however, is broken in the mean flow, as may be seen in (*b*)(i), where the central point of the flow field is slightly displaced from the centre of the H_l plane. Clear evidence of the broken S_r symmetry can be seen in (*c*)(i) where the flow is not symmetric about $z = 0$. The maximum values of the velocity components are: (i) $u_{max} = 1.2827$, $v_{max} = 0.2994$ and $w_{max} = 0.5660$; (ii) $u_{max} = 1.3239$, $v_{max} = 0.3263$ and $w_{max} = 0.6040$.

an amplitude of almost an order of magnitude smaller than all the other signals. Its frequency of oscillation is twice the fundamental frequency of the other temperature signals, as was confirmed by examining the Fourier spectrum of $T15$. These results are in excellent agreement with the numerical findings, and in particular, the same phase relationships between $T3$ and $T15$ are observed in both experiments and DNS, as can be seen in figure 9.

The numerical simulations offer the advantage that the complete flow field can be visualized, and, thus, they were used to gain insight into the oscillatory instability mechanism. The mean flow field was calculated for $Gr = 49\,000$ and $Pr = 0.019$ by averaging results over one period of oscillation. Subtracting the mean flow from the full results yielded the fluctuating flow field, which was saved every 1/16th of a period. A steady flow solution was also found numerically at $Gr = 49\,000$ by a stepwise increase of Gr up from $Gr = 39\,000$ in steps of $\Delta Gr = 1000$. A comparison between the flow fields of the two solutions is presented in figure 10. The mean velocity field of the oscillatory flow (figure 10(*a*)(i)–(*c*)(i)) and the steady velocity field (figure 10(*a*)(ii)–(*c*)(ii)) are visualized by projection onto the three principal planes, V_l, H_l and V_t. The mean flow of the oscillatory solution is clearly different from that reported by Henry &

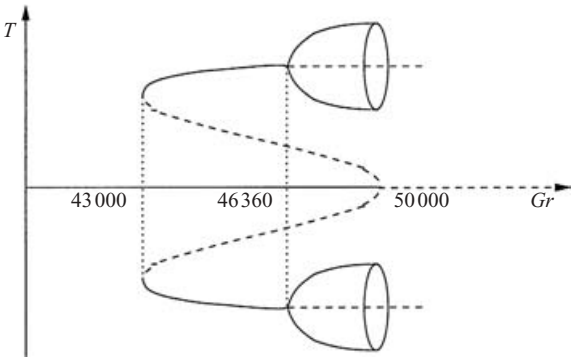

FIGURE 11. Schematic bifurcation diagram for the onset of oscillations in the three-dimensional numerical model. The solid (dashed) lines denote stable (unstable) states, respectively. The Hopf bifurcation occurs on the asymmetric steady branches, which are reached for increasing Gr through a subcritical symmetry-breaking pitchfork bifurcation. The given values of Gr are for $Pr = 0.019$.

Buffat (1998) for $Pr = 0$ and a cavity of relative dimensions $4 \times 2 \times 1$, i.e. of lesser widthwise confinement than in the present case. In Henry & Buffat's geometry, the mean flow was closely related to the two-dimensional result, with evidence of a transition to a multi-cell structure. By contrast, both the mean and the steady flow shown in figures 10(*a*)(i) and 10(*a*)(ii), which are for finite $Pr = 0.019$, consist of a large, single circulation, with a central region of strong shear. Complex secondary flows are observed which are characteristic of flows with finite-Prandtl-number values and relatively small lengthwise aspect ratios (see figures 10*b*,*c*). We refer to Juel *et al.* (2001) for a detailed description of these secondary flows.

The symmetry properties of the mean flow differ from the steady convective flow. While the steady flow field exhibits the π-rotational symmetry, S_r, about the y-axis as in figures 10(*b*)(ii) and 10(*c*)(ii), this symmetry is broken in the mean flow solution as in figures 10(*b*)(i) and 10(*c*)(i). The reflection symmetry, S, about the V_l plane is preserved in the mean flow as shown in figures 10(*b*)(i) and 10(*c*)(i), and in the steady flow alike, as shown in figures 10(*b*)(ii) and (*c*)(ii). The S_r asymmetry leads to a small displacement of the centre of the convective circulation towards either side.

The fact that the S_r symmetry is broken in the mean flow suggests that the Hopf bifurcation may have arisen on an asymmetric state. In fact, detailed numerical calculations starting from the oscillatory solution, and decreasing the Grashof number below the Hopf bifurcation point, indicate the existence of asymmetric steady states. Indeed, asymmetric states with opposite symmetries were obtained from independent calculations. For $Pr = 0.019$, the asymmetric solution is lost when the Grashof number is decreased from $Gr = 44\,000$ to $Gr = 43\,000$, whereas the Hopf bifurcation point was located at $Gr_c(\mathrm{num}) = 46\,360$. In addition, the oscillatory flow was initially reached by stepping the Grashof number directly to $Gr = 60\,000$. Indeed, as indicated above, a stepwise increase of Gr from $Gr = 39\,000$ showed that a transition from an S_r symmetric steady flow directly to the S_r asymmetric, oscillatory flow takes place at $Gr \simeq 50\,000$. The above evidence suggests that the transition to oscillatory flow takes place through a bifurcation sequence consisting of a subcritical symmetry-breaking bifurcation followed by a supercritical Hopf bifurcation on the asymmetric branches, as shown schematically in figure 11.

Experimentally, the steady flow appears to bifurcate directly and supercritically to a time-dependent state. However, it is likely that the symmetry about the y-axis of the

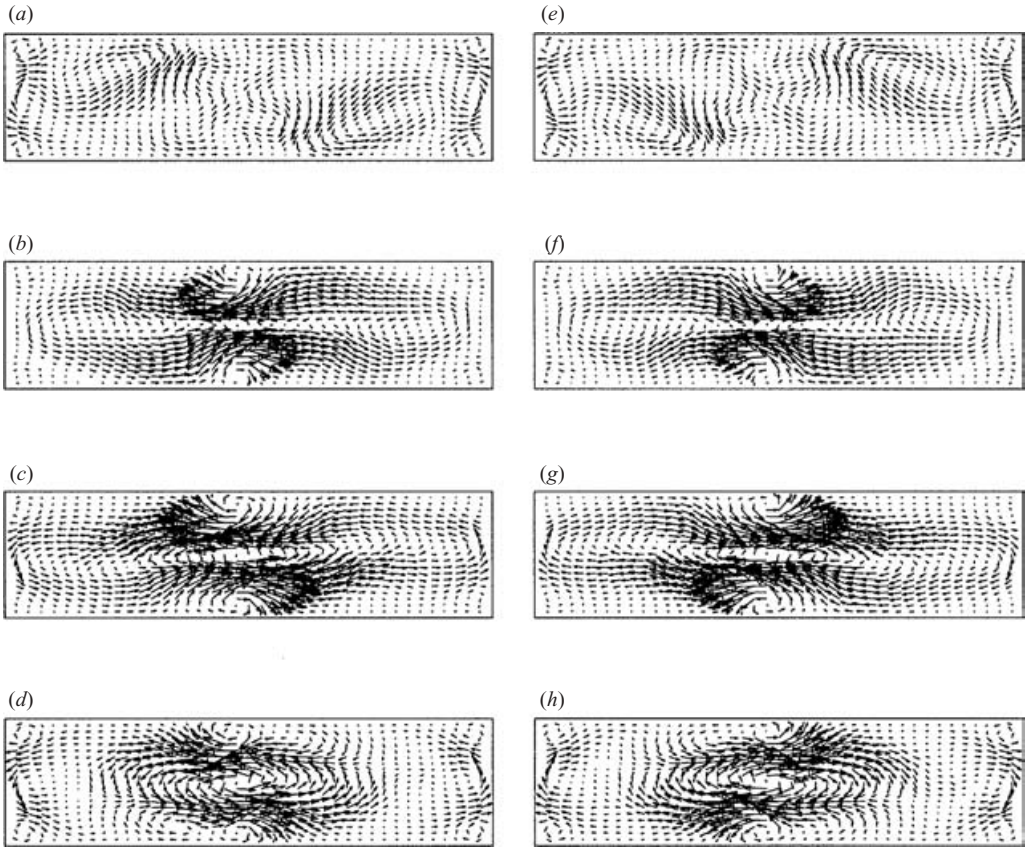

FIGURE 12. Fluctuating velocity field projected onto the H_l plane, and viewed from above: (*a*) $t=0$, (*b*) $t=T/8$, (*c*) $t=T/4$, (*d*) $t=3T/8$, (*e*) $t=T/2$, (*f*) $t=5T/8$, (*g*) $t=3T/4$, (*h*) $t=7T/8$. The parameters are $Gr=49\,000$, $Pr=0.019$.

numerical model does not exist in the experiment because it is naturally broken by non-Boussinesq perturbations. Indeed, despite the accurate experimental control of the boundary conditions discussed in § 3, the lack of S_r symmetry is inherent in the experiment and increases with Gr, owing to the monotonic variation of the material properties of gallium along the length of the enclosure. For instance, at $Gr=49\,100$ and $Pr=0.019$, the Prandtl number decreases by approximately 11% between the cold end and the hot end, the dynamic viscosity decreases by approximately 6.4% and the thermal conductivity by 5.3%. These are significant non-Boussinesq perturbations whose influence only becomes evident when focusing on the details of the transition to time-dependence. Thus, the subcritical S_r symmetry-breaking bifurcation is replaced by a continuous transition to a preferred asymmetric state, although based on the available experimental evidence, we cannot infer the detailed unfolding of the bifurcation.

The study of the oscillatory component of the flow field indicates that the Hopf bifurcation breaks the remaining reflection symmetry S. A symmetry-breaking Hopf bifurcation is characterized by an antisymmetric perturbation, and the oscillatory solution preserves the S symmetry between states separated by half-a-period, as discussed in detail by Henry & Buffat (1998). Consequently, the fluctuating flow field projected onto the H_l plane is found to be $T/2$ periodic, as shown in figure 12 with a sequence of snapshots sampled every eighth of a period.

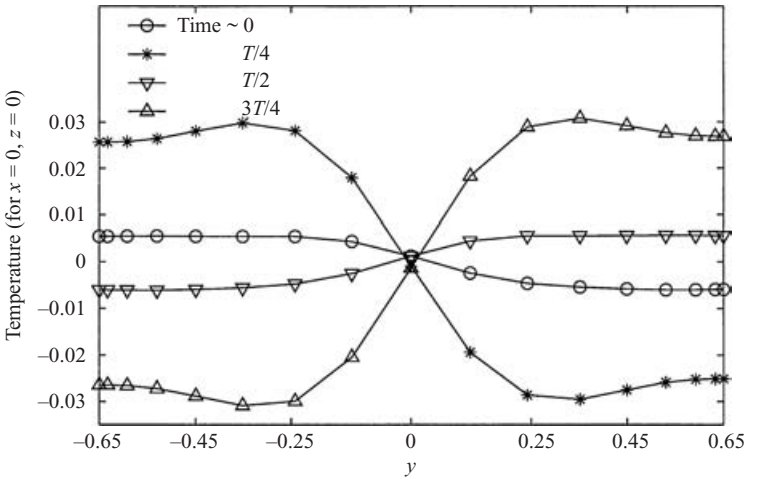

FIGURE 13. Temperature fluctuation profiles taken along y (width of the cavity). The parameters are $Gr = 50\,000$, $Pr = 0.019$.

In order to relate the oscillatory flow to the time series presented in figure 9, temperature fluctuation profiles sampled centrally ($x = 0$ and $z = 0$), across the width of the cavity, y, over a period of oscillations, are plotted in figure 13. Again, it is clear that the oscillatory state breaks the remaining reflection symmetry S about the V_l plane ($y = 0$). Thus, the temperature signal measured halfway across the cavity retains a small amplitude (which decreases to zero at onset), and it has twice the frequency of the signals measured elsewhere in the enclosure. The spatial distribution of the temperature oscillation shown in figure 13 has the form of a standing wave with a central node.

The spatial distribution of the temperature oscillation is a robust feature of low-Prandtl-number sidewall convective flows. Indeed, similar phase relationships were observed by Juel *et al.* (2001) for a bulk flow which presented a strong heat-loss-induced asymmetry about the y-axis, compared to the present flow where it has been minimized (see Hof *et al.* 2003). In both cases, however, the bulk flow preserves the symmetry about the V_l plane, which we have seen above is essential to observe the phase relationships displayed in figure 9. The experiments of Hart & Pratte (1990) in a cavity of relative dimensions $4 \times 2 \times 1$ also revealed that the temperature signals sampled in the V_l plane were dominated by the second harmonic of the frequency measured at off-centre positions. Although the origin of the oscillatory instability found in this study is different from that uncovered by Henry & Buffat (1998), both oscillatory transitions occur after an S symmetry breaking and the resulting oscillatory flows have similar characteristics. In particular, the phase relationships and the standing-wave character of the oscillatory mechanism appear to be a direct consequence of the S symmetry-breaking.

The rate of change of the total kinetic energy of the fluctuating flow was calculated directly as indicated in § 2. It can be separated into three contributions: shear of the mean flow, buoyancy and viscous dissipation. The rate of change of the total kinetic energy of the fluctuation, $\partial K/\partial t$, is plotted in figure 14(a), together with the three aforementioned contributions, for $Gr = 52\,900$, $Pr = 0.019$. The dominant production of fluctuating kinetic energy is due to the shear of the mean flow. The viscous dissipation term, which is always negative, acts to balance the destabilizing action of

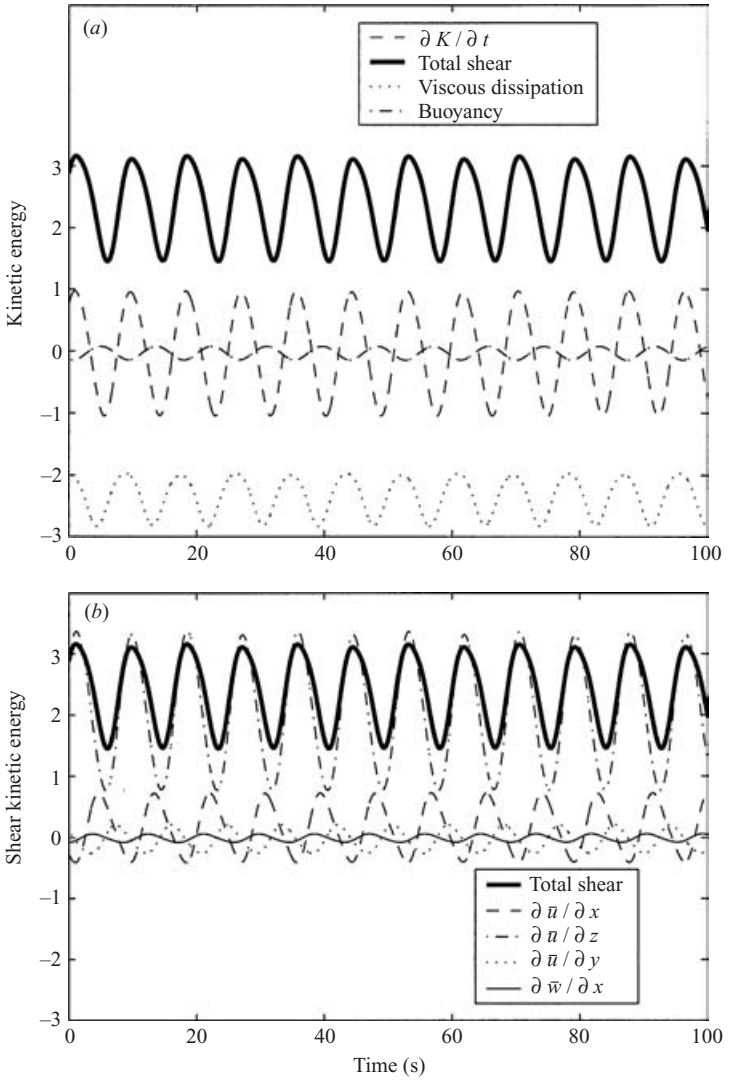

FIGURE 14. (*a*) Time series of the rate of change of the total kinetic energy and its components for $Gr = 52\,900$, $Pr = 0.019$: kinetic energy of the fluctuating flow due to shear of the mean flow, buoyancy, and viscous dissipation (see § 2 for the definitions of the different terms); (*b*) Comparison between the total shear energy of the fluctuating flow and its four largest components labelled in the legend by the corresponding mean flow gradient.

shear. The buoyancy contribution is approximately of an order of magnitude smaller, and oscillates between production and dissipation of kinetic energy.

The production of fluctuating kinetic energy by shear of the mean flow comprises nine parts, i.e. the gradients in each of the three directions of the three components of the mean velocity. The comparison between time series of the total shear energy and its four largest components, shown in figure 14(*b*), clearly indicates that the production of fluctuating kinetic energy by shear of the mean flow is essentially due to the term $w'(\partial\bar{u}/\partial z)u'$. This time series is the only one whose values are all positive, and it also has a total amplitude which is close to the total shear energy.

The above results demonstrate that the oscillatory flow is dominated by the shear of the mean flow, and primarily by the variation of the mean horizontal velocity with respect to the vertical direction. This suggests that the origin of the oscillatory instability is purely hydrodynamic. Finally, the production and dissipation of kinetic energy is concentrated in the central part of the cavity, around the region of high shear depicted in figure 10.

5. Conclusion

The results of an investigation into the transition to oscillatory flow in sidewall convection in molten gallium in a parallepiped cavity of dimensions $5.0 \times 1.3 \times 1.0$ have been presented. Direct comparison between numerical simulations of the three-dimensional Boussinesq model, and a carefully controlled experimental system, leads to a detailed understanding of the onset and spatial characteristics of the oscillatory flow. In addition, we were able to assess the validity of the Boussinesq approximation in a flow field which has practical significance. The onset of time-dependence takes place through supercritical Hopf bifurcations in both numerics and experiments. The critical thresholds are in good agreement and the loci of Hopf bifurcations in the (Gr, Pr)-plane are qualitatively similar.

However, the details of the bifurcation sequences leading to transition are different. In the numerical simulations, the steady flow first loses stability to a pair of S_r asymmetric states through a subcritical pitchfork bifurcation. It is then followed by supercritical Hopf bifurcations on the asymmetric branches. The absence of the steady S_r symmetry-breaking bifurcation in the experiment is attributed to non-Boussinesq perturbations which increase with Gr.

Importantly, however, the oscillatory flow itself is found to be robust despite the sensitivity of some characteristics to imperfections in boundary conditions. The oscillation is antisymmetric about V_l, so there is a 180° phase shift across the width of the cavity and the velocity field projected onto the V_l plane is $T/2$ periodic. Analysis of the energy contributions to the oscillatory flow suggests that the instability is purely hydrodynamic in nature, and arises because of the high shear in the central part of the cavity. The numerical and experimental frequencies of oscillation close to onset are in excellent agreement.

The authors wish to thank Dr S. Tavener for useful discussions on the bifurcation structure. This work was funded by the EPSRC (B. H.), a visiting fellowship to Ecole Centrale de Lyon (A. J.), an Alliance Partnership grant from the British Council and Egide (A. J., D. H.), a fellowship from the Région Rhône–Alpes (L. Z.), and an EPSRC 'Senior Fellowship' (T. M.). Support from the Centre National des Etudes Spatiales (CNES) is also gratefully acknowledged. The computations were carried out on a NEC-SX5 computer, with the support of the Centre National de la Recherche Scientifique (CNRS) through the Institut du Développement et des Ressources en Informatique Scientifique (IDRIS).

REFERENCES

Afrid, M. & Zebib, A. 1990 Oscillatory three-dimensional convection in rectangular cavities and enclosures. *Phys. Fluids* A **2**, 1318–1327.

Ben Hadid, H. & Henry, D. 1997 Numerical study of convection in the horizontal Bridgman configuration under the action of a constant magnetic field. Part 2: Three-dimensional flow. *J. Fluid Mech.* **333**, 57–83.

Brandes, E. A. & Brook, G. B. (ed.) 1992 *Smithells Metals Reference Book*. 7th edn. Butterworths/Heinemann.

Braunsfurth, M. G. & Mullin, T. 1996 An experimental study of oscillatory convection in liquid gallium. *J. Fluid Mech.* **327**, 199–219.

Braunsfurth, M. G., Skeldon, A. C., Juel, A., Mullin, T. & Riley, D. 1997 Free convection in liquid gallium. *J. Fluid Mech.* **342**, 295–314.

Gill, A. E. 1974 A theory of thermal oscillations in liquid metals. *J. Fluid Mech.* **64**, 577–588.

Hart, J. E. 1972 Stability of thin non-rotating Hadley circulations. *J. Atmos. Sci.* **29**, 687–697.

Hart, J. E. 1983 A note on the stability of low-Prandtl-number Hadley circulations. *J. Fluid Mech.* **132**, 271–281.

Hart, J. E. & Pratte, J. M. 1990 A laboratory study of oscillations in differentially heated layers of mercury. In *Numerical Simulation of Oscillatory Convection in Low-Pr Fluids* (ed. B. Roux), *GAMM Workshop*. Notes on Numerical Fluid Mechanics, vol. 27. Vieweg.

Henry, D. & Buffat, M. 1998 Two- and three-dimensional numerical simulations of the transition to oscillatory convection in low-Prandtl number fluids. *J. Fluid Mech.* **374**, 145–171.

Hof, B., Juel, A. & Mullin, T. 2003 Magnetohydrodynamic damping of convective flows in molten gallium. *J. Fluid Mech.* **482**, 163–179.

Hof, B. & Mullin, T. 2001 Critical dynamics in oscillatory convection. *Magnetohydrodynamics* **37**, 119–126.

Hung, M. C. & Andereck, C. D. 1988 Transitions in convection driven by a horizontal temperature gradient. *Phys. Lett.* A **132**, 253–258.

Hung, M. C. & Andereck, C. D. 1990 Subharmonic transition in a moderately shallow cavity. In *Numerical Simulation of Oscillatory Convection in Low-Pr Fluids* (ed. B. Roux), *GAMM Workshop*. Notes on Numerical Fluid Mechanics, vol. 27. Vieweg.

Hurle, D. T. J. 1966 Temperature oscillations in molten metals and their relationship to growth striae in melt-grown crystals. *Phil. Mag.* **13**, 305–310.

Hurle, D. T. J., Jakeman, E. & Johnson, C. P. 1974 Convective temperature oscillations in molten gallium. *J. Fluid Mech.* **64**, 565–576.

Juel, A., Mullin, T., Ben Hadid, H. & Henry, D. 2001 Three-dimensional free convection in molten gallium. *J. Fluid Mech.* **436**, 267–281.

Kamotani, Y. & Sahraoui, T. 1990 Oscillatory natural convection in rectangular enclosures filled with mercury. *J. Heat Transfer* **112**, 235–255.

Karniadakis, G. E., Israeli, M. & Orszag, S. A. 1991 High-order splitting method for the incompressible Navier–Stokes equations. *J. Comput. Phys.* **97**, 414–443.

Kaye, G. W. & Laby, T. H. 1982 *Tables of Physical and Chemical Constants*, 14th Edn. Longman.

Kuo, H. P. & Korpela, S. A. 1988 Stability and finite amplitude natural convection in a shallow cavity with insulating top and bottom and heated from a side. *Phys. Fluids* **31**, 33–42.

Laure, P. 1987 Etude des mouvements de convection dans une cavité rectangulaire soumise à un gradient de température horizontal. *J. Méc. Théor. Appl.* **6**, 351–382.

Laure, P. & Roux, B. 1990 Linear and nonlinear analysis of the Hadley circulation. In *Numerical Simulation of Oscillatory Convection in Low-Pr Fluids* (ed. B. Roux), *GAMM Workshop*. Notes on Numerical Fluid Mechanics, vol. 27. Vieweg.

March, N. H. 1968 *Liquid Metals*. Pergamon.

Mills, K., Monaghan, B. & Keene, B. 1996 Thermal conductivities of molten metals: Part 1 pure metals. *Intl Materials Rev.* **41**, 209–242.

Müller, G. & Ostrogorsky, A. 1993 Convection in melt growth. In *Handbook of Crystal Growth: Growth Mechanisms and Dynamics*, vol. 2b (ed. D. T. J. Hurle). North-Holland.

Pratte, J. M. & Hart, J. E. 1990 Endwall driven, low Prandtl number convection in a shallow rectangular cavity. *J. Cryst. Growth* **102**, 54–68.

Roux, B. (ed.) 1990 *Numerical Simulation of Oscillatory Convection in Low-Pr Fluids*, *GAMM Workshop*. Notes on Numerical Fluid Mechanics, vol. 27. Vieweg.

Skeldon, A. C., Riley, D. C. & Cliffe, K. A. 1996 Convection in a low Prandtl number fluid. *J. Cryst. Growth* **162**, 95–106.

Smithells, C. J. & Brandes, E. A. (ed.) 1976 *Metals Reference Book*, 5th edn. Butterworths.

Strogatz, S. H. 1994 *Nonlinear Dynamics and Chaos*. Addison-Wesley.

Touloukian, Y. S., Powell, R. W., Ho, C. Y. & Klemans, P. G. (ed.) 1979 *Thermophysical Properties of Matter, Vol.1: Thermal Conductivity: Metallic Elements and Alloys*. IFI/Plenum.

Wakitani, S. 2001 Numerical study of three-dimensional oscillatory natural convection at low Prandtl number in rectangular enclosures. *J. Heat Transfer* **123**, 77–83.

Wang, T. M. & Korpela, S. A. 1989 Convection rolls in a shallow cavity heated from a side. *Phys. Fluids* A **1**, 947–953.

Winters, K. H. 1988 Oscillatory convection in liquid metals in a horizontal temperature gradient. *Intl J. Numer. Meth. Engng* **25**, 401–414.